

# A Digital Filtering ADC With Programmable Blocker Cancellation for Wireless Receivers

Qiwei Wang<sup>ID</sup>, Student Member, IEEE, Hajime Shibata<sup>ID</sup>, Member, IEEE, Antonio Liscidini, Senior Member, IEEE, and Anthony Chan Carusone, Senior Member, IEEE

**Abstract**—This paper presents a long-term evolution (LTE) receiver (RX) front end with a digital filtering analog to digital converter (ADC) in the baseband to perform multi-band blocker cancellation. The digital filtering ADC has a digitally defined transfer function that is highly reconfigurable and insensitive to PVT variations. The dynamic range requirement of the blocker cancellation feedback digital to analog converter (DAC) is relaxed with a trivial uncalibrated first-order passive high-pass filter. The programmable digital filter provides 34.9-dB attenuation of transmitter leakage and variable attenuation of an additional blocker anywhere in the frequency range 17.5–107.5 MHz. A blocker detection algorithm for this RX is presented and takes approximately 26  $\mu$ s to converge. The RX front end operates at 1.8 GHz with a noise figure of 3.9 dB and IIP3 of  $-5$  dBm, and consumes only 20.4–37.5 mW, the lowest among the state-of-the-art designs.

**Index Terms**—Analog to digital converter (ADC), baseband, blocker, digital, digital to analog converter (DAC), filtering, long-term evolution (LTE), reconfigurable, wireless receiver (RX).

## I. INTRODUCTION AND BACKGROUND

LOW supply voltages and analog gain in nanoscale CMOS make the design of a RF receiver (RX) very challenging. One of the most difficult requirements is to reject signals in frequency bands adjacent to the channel of interest (blockers), whose amplitude is much larger than the in-band signal.

Traditionally, an analog low pass filter (LPF) is used before the analog to digital converter (ADC) in the baseband to provide blocker filtering, as shown in Fig. 1. To improve power efficiency, the LPF and ADC can be combined into a global feedback loop thus creating an analog filtering ADC. There are two approaches to designing an analog filtering ADC. The first embeds the analog filter inside the feedback loop of the ADC, thus relaxing the filter's noise and distortion requirements [1], [2]. The second approach moves the ADC inside the feedback loop of the analog filter, relaxing the ADC thermal and quantization noise requirements [3]–[6].

Seeking the benefits of a more digital implementation, ADCs with digitally improved blocker rejection were proposed in [7] and [8], where a digital filter is incorporated within

Manuscript received July 10, 2017; revised September 14, 2017, October 8, 2017, and October 17, 2017; accepted October 19, 2017. Date of publication November 20, 2017; date of current version February 21, 2018. This paper was approved by Guest Editor Rikky Muller. This work was supported by Analog Devices. (Corresponding author: Qiwei Wang.)

Q. Wang, A. Liscidini, and A. C. Carusone are with the University of Toronto, Toronto, ON M5S 2E4, Canada (e-mail: jeffrey.wang@isl.utoronto.ca).

H. Shibata is with Analog Devices, Toronto, ON M5G 2C8, Canada.

Color versions of one or more of the figures in this paper are available online at <http://ieeexplore.ieee.org>.

Digital Object Identifier 10.1109/JSSC.2017.2766213

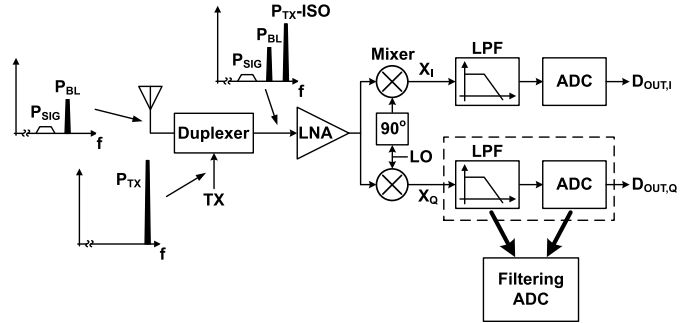


Fig. 1. Block diagram of a typical wireless RX, with a TX and a duplexer to illustrate the blocker profile.

a feedback loop around the ADC to enhance the signal transfer function (STF) roll-off of a third-order continuous-time  $\Delta\Sigma$  modulator (CTDSM). The inclusion of the digital filter increased the blocker attenuation by 6 dB and also reduced the requirements on the first integrator. Although this approach gives the impression of a more digital and flexible implementation, the filter transfer function is still determined by the poles of the analog circuitry hence limiting filter selectivity and requiring accurate calibration and PVT correction.

This paper presents a digital filtering ADC, which has a digitally defined transfer function that is highly reconfigurable and completely insensitive to PVT variations [9]. The digital blocker cancellation path provides a maximum blocker attenuation of 34.9 dB. Noise and distortion introduced in the blocker cancellation feedback digital to analog converter (DAC) are high-pass filtered with a trivial uncalibrated first-order passive network. As a result, the analog baseband circuitry consists only of the first-order CTDSM, a feedback DAC with relaxed specifications, plus a few passive components that do not require tuning. The resulting RX is low-power and well-suited for implementation in CMOS technologies at 28 nm and beyond.

## II. BASEBAND DIGITAL FILTERING ADC

The specification of a wireless RX based on transmitter (TX) leakage and blocker power is shown in Fig. 2. The sensitivity test and blocking test are worst case scenarios for a wireless RX, where the desired signal is very small and the TX leakage and blocker power are high. However, a more common scenario is in the bottom left corner, where the TX leakage and blocker power are moderate. Designing a wireless

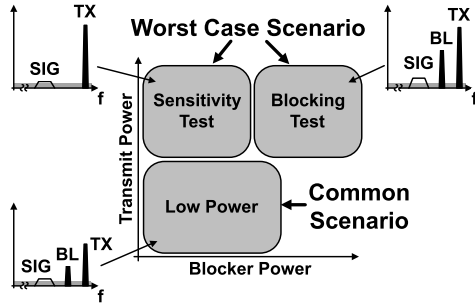


Fig. 2. Specification of a wireless RX, based on TX leakage and blocker power.

RX working in this region is trivial. A typical wireless RX is designed to work in the worst case scenarios. In this paper, we are targeting a highly reconfigurable RX that works in the worst case scenarios, but can also take advantage of the common scenario to save power.

Typically, the biggest blocker comes from the local TX. For example, in the long-term evolution (LTE) standard, TX leakage can be as high as  $-30$  dBm at the RX front end assuming a TX-RX isolation of  $57$  dB and TX-antenna insertion loss of  $2$  dB [10]. Fortunately, TX leakage appears at a known frequency offset—a minimum of  $41$  MHz in band 20. Additionally, one other blocker (or two in an IMD test) may be present, as shown in Fig. 1.

A starting point for the digital filtering ADC is shown in Fig. 3(a), where a digital low-pass filter is placed after the ADC to attenuate the blockers. However, the ADC needs to have a high dynamic range, because it needs to handle the large blocker without saturating. A digital high-pass filter (HPF) in feedback, in combination with a DAC, can be used to reconstruct the blocker and cancel it at the summing node in front of the ADC [see Fig. 3(b)]. As a result, the ADC's dynamic range requirement is reduced. However in this case, at high frequency, the digital filter gain never rolls off, and the phase shift contributed by the ADC and the digital filter becomes significant; hence, the feedback loop becomes unstable. To make the loop stable, high-frequency loop gain can be reduced by replacing the digital HPF with a digital bandpass filter [see Fig. 3(c)]. Blockers are still canceled within the bandwidth of the digital bandpass filter. In the case where more than one blocker is present, multiple bandpass filters can be placed in parallel [see Fig. 3(d)], each responsible for one blocker. The proposed digital filtering ADC is easily reconfigurable, and the digital filters can be turned off when there are no blockers to save power.

A second-order digital bandpass filter in feedback is used which makes the closed loop response a second-order notch filter. The resulting closed-loop magnitude response for notch filters with different center frequencies is plotted in Fig. 4(a). They all have the same  $Q$  factor of  $24$ , and the peak attenuation is adjusted such that the gain at the signal band edge,  $B$ , is  $-1$  dB. Assuming that there is only one blocker present, and the center frequency of the notch can be placed exactly at the blocker frequency, the effective attenuation of the second-order notch filter is plotted for continuous wave (CW) blockers

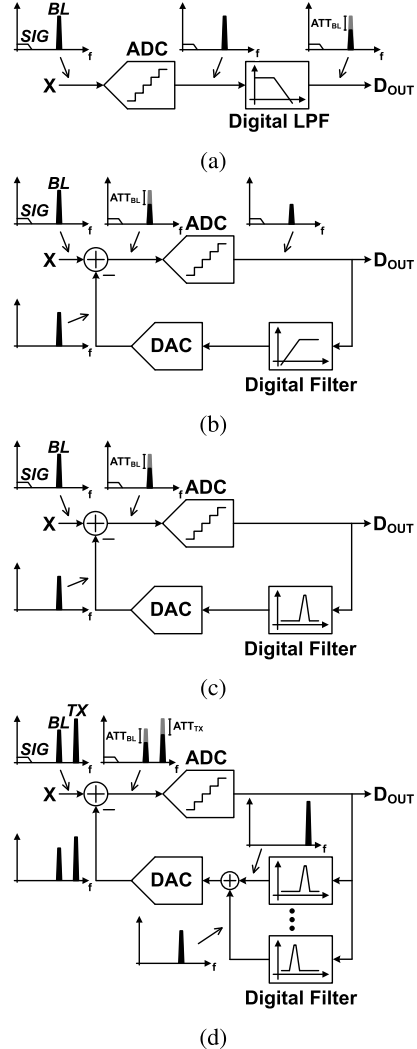
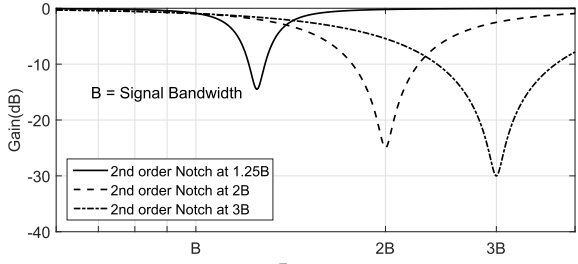


Fig. 3. Block diagram of a digital filtering ADC with (a) low pass filter after the ADC, (b) HPF in feedback, (c) bandpass filter in feedback, and (d) multiple bandpass filters in feedback.

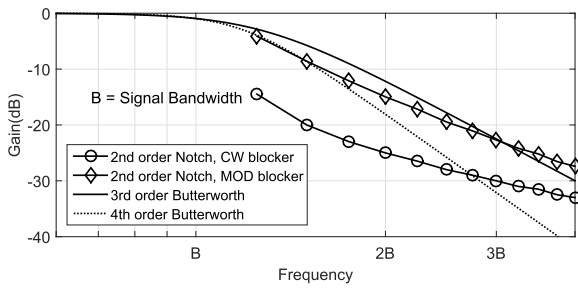
and modulated blockers in Fig. 4(b). The attenuation of the modulated blocker is calculated based on the average attenuation over a bandwidth of  $B/2$ . It can be seen that the second-order notch filter provides much more attenuation of nearby narrowband CW blockers than a fourth-order Butterworth filter, and an attenuation of modulated blockers similar to a third-order Butterworth filter.

The baseband architecture with digital multi-band blocker cancellation is shown in Fig. 5. The baseband circuitry receives a current-mode signal comprised of the in-band signal (SIG), TX leakage, and an additional blocker (BL). A digital bandpass filter extracts the TX leakage at its known frequency offset, while a programmable digital bandpass filter can be used to track another blocker. The programmable filter can be set to reject blockers at any frequency offset in the range  $17.5$ – $107.5$  MHz under the control of a blocker detection algorithm. The DAC converts the summed digital filter outputs to an analog current.

The DAC requires sufficient DR to cancel full-scale TX leakage and blockers while contributing minimal noise in



(a)



(b)

Fig. 4. (a) Simulated transfer function of the second-order notch filters at different center frequencies with  $Q = 24$ . (b) Attenuation of the second-order notch filters for a CW blocker and a modulated blocker, compared with third- and fourth-order Butterworth filter.

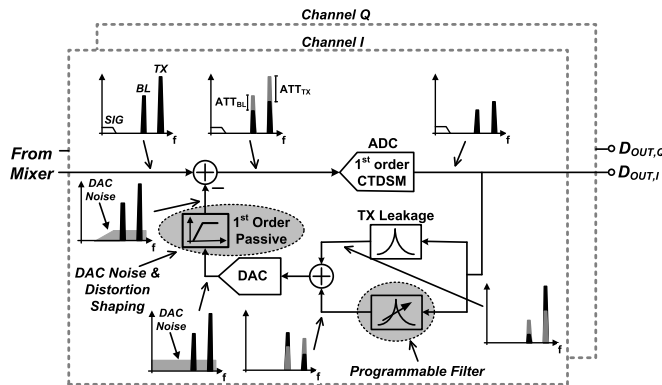
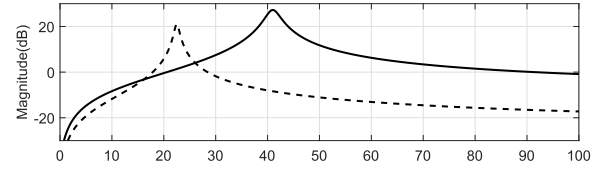


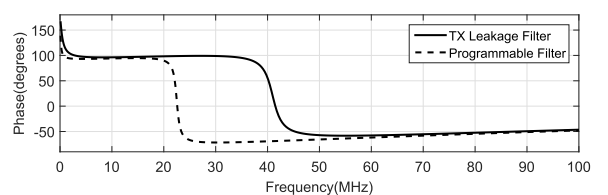
Fig. 5. Baseband signal flow with digital multi-band blocker cancellation.

the signal band. Here, recognizing that the DAC is used to replicate blockers and does not have any signal content in the band of interest, the first-order passive HPF is placed at the DAC output to reduce in-band thermal noise, quantization noise, and distortion from the DAC. Hence, in this paper, a 5-bit DAC provides 34.9-dB blocker attenuation and its DR is not a limiting factor. Only the first-order CTDSM ADC is needed in the main signal path because most of the blocker power is already canceled by the digital path and DAC.

Fig. 6(a) shows the simulated transfer function of the implemented digital bandpass filters programmed to cancel a blocker at 22.5 MHz and the TX leakage at 41 MHz. The closed loop transfer function is shown in Fig. 6(b). The delays from the ADC and the digital logic translate to an increasing phase shift versus frequency. As a result, the loop phase margin will get worse as the center frequency of the digital bandpass



(a)



(b)

Fig. 6. Simulated transfer function of (a) digital bandpass filters for TX leakage and additional blocker and (b) closed loop transfer function.

filter increases. Therefore, the maximum center frequency of the programmable filter is limited to 107.5 MHz. The center frequency could be increased further by decreasing the filter gain (providing less blocker attenuation) or increasing the filter  $Q$  factor.

An architecture similar to Fig. 3(c) was first proposed in [8], with two differences. First, the digital bandpass filter in [8] was used to assist the STF roll-off of a third-order CTDSM and increased blocker suppression by 6 dB. Since the filter transfer function still relies on the poles of the analog path, accurate calibration and PVT correction are needed. In this paper, the filter transfer function depends entirely on the digital bandpass filter which is very accurate. Second, without the first-order passive HPF at the DAC output, the dynamic range required of the DAC in [8] was very high. In addition to the consequently low thermal noise and distortion requirements on the DAC, in the presence of strong blockers, DAC clock jitter in [8] will contribute significant noise in the signal band. Moreover, to mitigate the quantization noise from the DAC, an off-chip reconstruction filter that matches the transfer function of the analog path was needed in [8].

### III. BASEBAND BLOCKER DETECTION

In this section, a blocker detection algorithm that tracks the blocker location in real time is proposed allowing the RX to adapt to changing channel conditions. There are two requirements for the blocker detection algorithm. First, the time required for blocker detection must be much smaller than the rate of change in the channel conditions. Second, the blocker frequency needs to be accurately detected as any uncertainty in the blocker frequency will lower the effective blocker attenuation due to the filter's high  $Q$  factor.

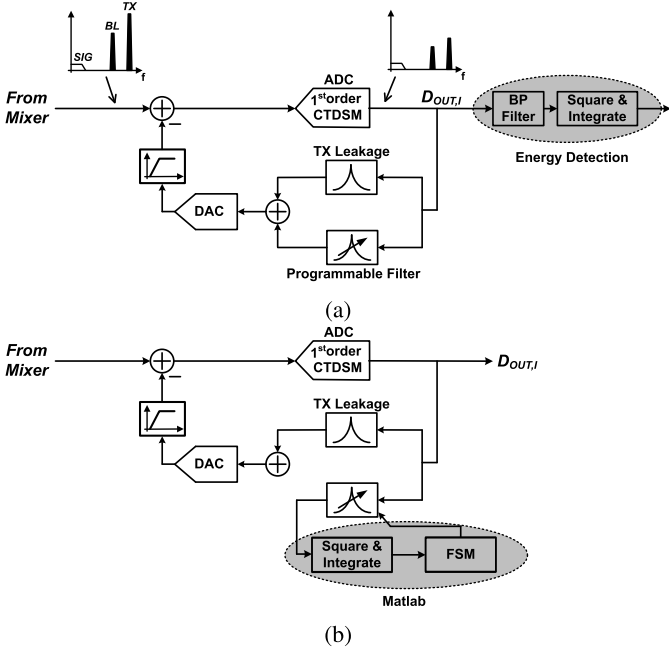


Fig. 7. Block diagram of (a) narrowband spectrum sensing (b) implemented blocker detection with programmable digital filter reused.

To compensate the rapid and significant variations in the channel conditions, the LTE standard provides an automatic repeat request (ARQ) [11]. In an ARQ scheme, for every block of data 1 ms in length, the RX relies on error detection to detect uncorrectable errors. If uncorrectable errors exist, the RX can ask for the TX to retransmit the same information. The block with errors is preserved and combined with the retransmitted block to increase the effective SNR. In this paper, the block length of 1 ms is assumed to be the maximum time allowable for the blocker detection algorithm.

Blocker detection can be considered as a spectrum sensing problem, where the spectrum at the ADC output needs to be sensed and the frequency of the largest blockers needs to be detected. A popular narrowband spectrum sensing algorithm in cognitive radio networks is energy detection [12], as shown in Fig. 7(a). A bandpass filter followed by a square and integrate block is used to calculate the total power in the narrowband that is defined by the bandpass filter. It has the advantage of lower implementation and computational complexity compared to other narrowband spectrum sensing techniques [12]. If the center frequency of the bandpass filter is swept, wideband spectrum sensing is achieved. The block diagram for blocker detection mode is shown in Fig. 7(b) where the programmable digital bandpass filter is disconnected from the main loop and reused for energy detection. Therefore, the only extra hardware is the square and integrate block and the finite state machine (FSM) which is implemented off-chip in MATLAB for this prototype. If implemented on-chip, this additional digital logic will increase the total digital circuit area by 15%.

The programmable digital bandpass filter is swept over the frequency range from 17.5 to 107.5 MHz and the simulated magnitude responses are shown in Fig. 8. The  $Q$  factor of

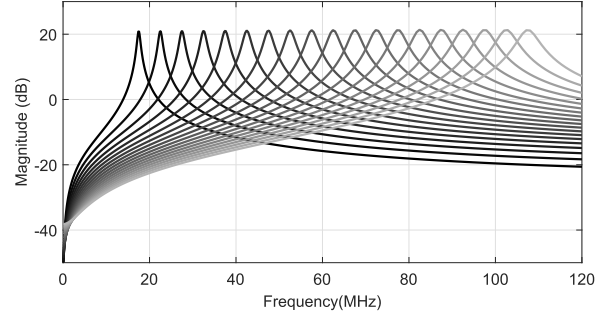


Fig. 8. Simulated magnitude responses for the swept programmable digital bandpass filter.

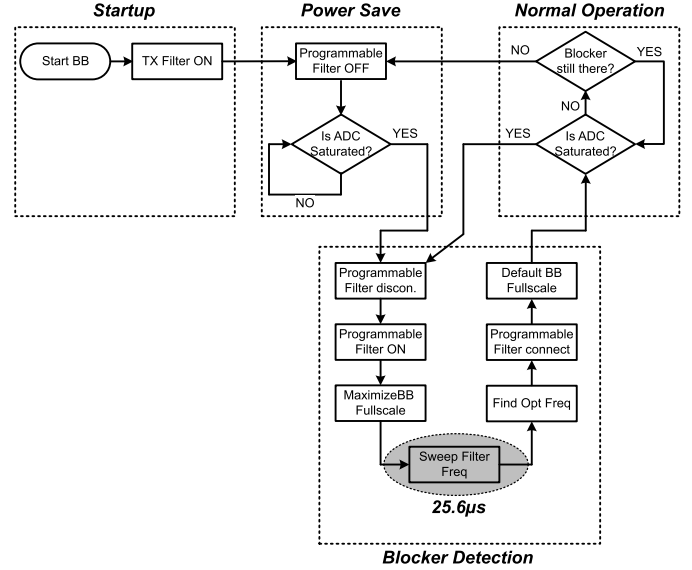


Fig. 9. FSM of the blocker detection algorithm.

the filter is 24. For each frequency setting, the digital filter starts in the reset state, and runs for 400 samples to obtain an accurate power estimate.

The state diagram of the blocker detection algorithm is shown in Fig. 9. The baseband starts in the initial state, where the bandpass filter responsible for the TX leakage is turned on. Note that for LTE, the TX leakage appears at a known frequency offset, and no blocker detection is needed for the TX leakage. The next state is the power save state, where the programmable filter is turned off and the ADC output is continuously monitored to detect saturation from a new blocker. When the ADC is saturated, the probability of the maximum code and minimum code at the quantizer output (for a 17-level quantizer, it would be +8 and -8) increases significantly. The ADC saturation criteria are implemented by monitoring the number of +8 and -8 outputs from the quantizer within every 400 samples.

In the case where the ADC saturates, it means that a blocker is present and the blocker detection algorithm starts. First, the baseband full scale is maximized to bring the ADC out of saturation, with a small noise penalty. The center frequency of the bandpass filter is swept in 1 MHz increments from 17.5 to 107.5 MHz, taking a total of 36400 samples which translate

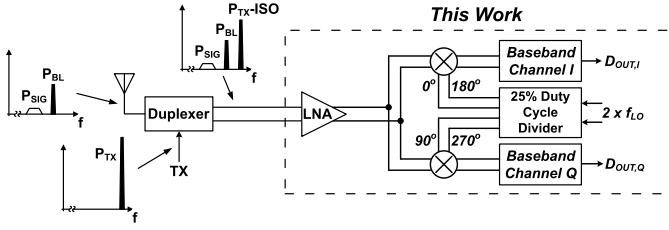


Fig. 10. Top-level block diagram of the proposed wireless RX, with a TX and a duplexer to illustrate the blocker profile.

to  $50.6 \mu\text{s}$  at an ADC sampling frequency of  $720 \text{ MHz}$ . The algorithm time can be cut in half to  $25.6 \mu\text{s}$  by using both the I and Q channels of the baseband, since they see the same channel conditions. The frequency setting with the most power is the blocker frequency and the programmable digital filter is programmed to that setting and connected to the main feedback loop to cancel the blocker. The total blocker detection algorithm takes approximately  $26 \mu\text{s}$  and it is dominated by the filter frequency sweep time. Note that this time is much less than the transport block size of  $1 \text{ ms}$  in LTE. After the blocker is detected and canceled, the baseband goes into normal operation, where the ADC output is continuously monitored in case the blocker frequency changes. The blocker power is also monitored at the output of the programmable filter to ensure that the baseband goes into power save mode when the blocker disappears.

#### IV. CIRCUIT IMPLEMENTATIONS

The top-level block diagram of the proposed wireless RX prototype is shown in Fig. 10. An RF front end is designed and included to test the blocker cancellation of the baseband in a realistic scenario. The low input-referred noise of this baseband permits a simplified and low-power low-noise amplifier (LNA) design. A common-gate LNA with a differential input impedance of  $50 \Omega$  is used, as shown in Fig. 11(a). To improve its transconductance, the NMOS input pair is capacitively cross-coupled [13], and the differential input is also fed into the gate of the PMOS input pair. The LNA output impedance is improved with cascode NMOS and PMOS devices. The off-chip balun, which provides the single-ended to differential conversion, is also used to provide the dc bias current to the LNA input. The I and Q current-mode passive mixers are driven by a 25% duty cycle divider that consists of two latches [14] [see Fig. 11(b)]. The divider outputs 75% duty cycle clock phases which are converted to 25% duty cycle clocks by an inverter. A 50% duty cycle clock at twice the local oscillator (LO) frequency is provided to the divider from off-chip.

Fig. 12 shows the detailed baseband circuit design. Since the mixer outputs a current mode signal, the first-order passive low-pass filter with 20-MHz cutoff frequency is realized simply by  $R_0$  and  $C_0$ . The passive low-pass filter acts as an anti-aliasing filter and also provides some attenuation of out-of-band blockers. The voltage swings at the mixer output  $I_{IN,I}$  and  $I_{IN,Q}$  are determined by the product of the mixer output current and  $R_0$ . Therefore, a small  $R_0$  ( $100 \Omega$ ) is

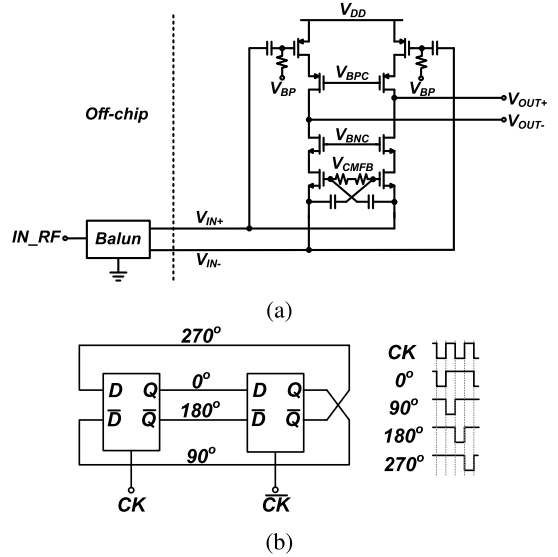


Fig. 11. RF front-end building blocks. (a) LNA implementation. (b) 25% duty cycle divider.

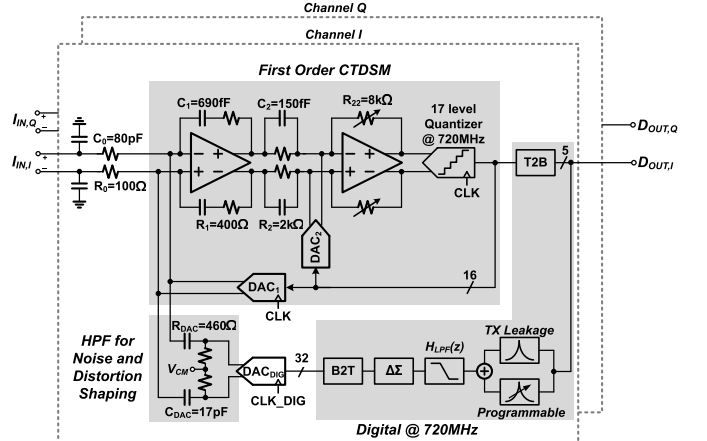


Fig. 12. Baseband circuit design with the first-order CTDSM, digital circuit, and HPF highlighted.

used to improve the mixer linearity. However, the small series impedance formed by  $R_0$  and  $C_0$  increases the noise contribution of the first amplifier. The first operational amplifier is the integrator while the second operational amplifier acts as a variable gain amplifier (VGA) and allows for excess loop delay compensation with DAC<sub>2</sub> [15]. A zero is added by introducing  $C_2$  to extend the bandwidth of the VGA. Otherwise, the phase shift of the VGA will cause peaking in the noise transfer function. The baseband has an input bandwidth of  $9 \text{ MHz}$  (consistent with LTE20) with the quantizer clocked at  $720 \text{ MHz}$  yielding an oversampling ratio of 40. The quantizer has 17 levels to ensure acceptable levels of quantization noise and sensitivity to clock jitter. Since this baseband has a relatively few gain stages (2) compared to traditional RX designs, pre-amplifiers precede the quantizer comparators to reduce their input-referred noise and mismatch.

The detailed digital feedback filter implementation running at  $720 \text{ MHz}$  is shown in Fig. 13. The 16-bit thermometer coded

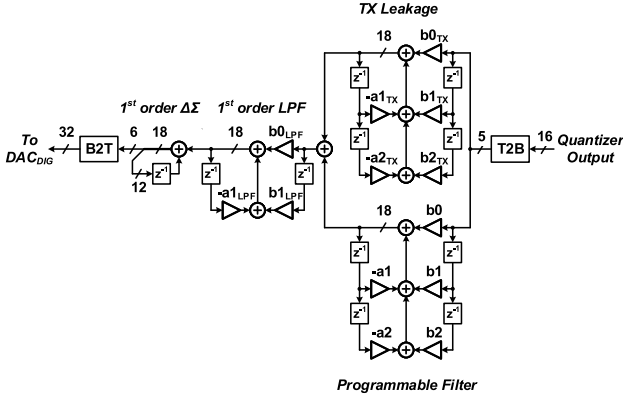


Fig. 13. Detailed digital circuit implementation.

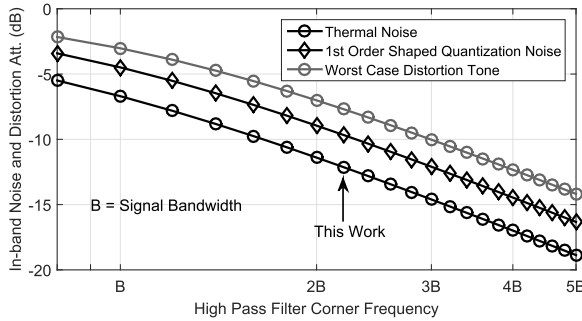


Fig. 14. Simulated DAC in-band noise and distortion suppression as a function of HPF corner frequency.

quantizer output is first converted to a 5-bit binary code with a thermometer to binary decoder (T2B) which is implemented using Wallace tree adders. Two digital second-order infinite impulse response (IIR) filters with 9-bit coefficient resolution detect and cancel TX leakage and one additional blocker. Note that in an intermodulation test, where TX leakage plus two additional blockers are present, canceling the TX leakage and the blocker at lower offset frequency is sufficient to reduce the intermodulation product significantly. The fully programmable coefficients allow accurate adjustment of the filter center frequency, gain, and  $Q$  factor to effectively cancel blockers at different frequencies, power levels, and modulation bandwidth. The output of both IIR filters is rounded to 18 bits to achieve a balance between hardware complexity and rounding error. The result is further truncated to 6 bits at the input of the binary to thermometer encoder (B2T) where the resulting quantization noise is shaped by the first-order delay-less digital  $\Delta\Sigma$  modulator.

The output noise and distortion from DAC<sub>DIG</sub> are shaped further by the first-order passive HPF created by  $R_{DAC}$  and  $C_{DAC}$ . The value of  $R_{DAC}$  is chosen to be much larger than  $R_0$  to minimize the effects of the HPF on the feedback factor of the first amplifier. Fig. 14 shows the simulated DAC in-band noise and distortion suppression as a function of HPF corner frequency. The corner frequency is presented as a function of the signal bandwidth  $B$ . The worst case distortion tone attenuation is calculated at the signal band edge where the HPF introduces the least attenuation. The thermal noise,

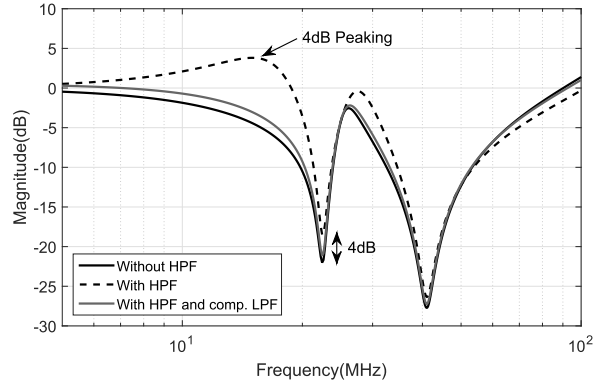


Fig. 15. Simulated closed-loop magnitude response with the LPF used to compensate the HPF.

quantization noise, and worst case distortion suppression with a corner frequency of 2.2 times the signal bandwidth are 12.1, 9.7, and 7.7 dB, respectively.

The first-order passive HPF with transfer function  $H_{HPF}(s)$  modifies the open loop gain of the system and thus introduces 4 dB peaking and 4 dB less blocker attenuation, as shown in Fig. 15. The first-order digital IIR LPF ( $H_{LPF}(z)$ ) with dc gain of 26 dB, a pole at 1 MHz, and a zero at 20 MHz is added to compensate the HPF. It is designed such that the magnitude of  $H_{HPF}(s) \cdot H_{LPF}(z)$  is approximately unity from 1 to 360 MHz.

The three DACs are designed using a high-speed current-steering architecture [16]. No mismatch shaping is needed for DAC<sub>1</sub>, because it does not need to handle the blockers. For DAC<sub>DIG</sub>, the HPF is sufficient to filter distortion caused by DAC nonlinearity. Dither is not used in the DACs. The unit current for DAC<sub>1</sub>, DAC<sub>2</sub>, and DAC<sub>DIG</sub> is 1.6, 1.4, and 7  $\mu$ A respectively. DAC<sub>DIG</sub> is clocked by CLK<sub>DIG</sub>, which is delayed from CLK by 0.7 period. The baseband full scale can be adjusted in 1 dB steps by increasing the unit current in DAC<sub>1</sub>, DAC<sub>2</sub>, and DAC<sub>DIG</sub>, and decreasing the VGA gain by the same amount.

A third-order feed-forward amplifier is used for the first operational amplifier [see Fig. 16(a)]. The first stage consumes 53% of the opamp power to reduce the input referred noise, whereas the output stage consumes only 20% of the opamp power, since the blocker power is mostly canceled by the digital path. A compensation capacitance  $C_C$  is placed at the output of the first stage to reduce the bandwidth of the third-order path. It is also possible to compensate the first stage with a Miller capacitor to reduce the compensation capacitor size. Three low-speed common mode feedback (CMFB) circuits are used to produce bias voltages  $V_{CM1}$ ,  $V_{CM2}$ , and  $V_{CM3}$  for the three stages, with the schematic of the second stage CMFB shown in Fig. 16(b). To protect the amplifier from high-frequency common mode noise, mainly from the supply voltage ripples amplified by the PMOS pseudo differential pair, the CMFB circuit has a bandwidth of approximately 360 MHz. The differential output of the second stage  $V_{O2+}$  and  $V_{O2-}$  is averaged using a source follower, and common mode current is injected back into  $V_{O2+}$  and  $V_{O2-}$  with a

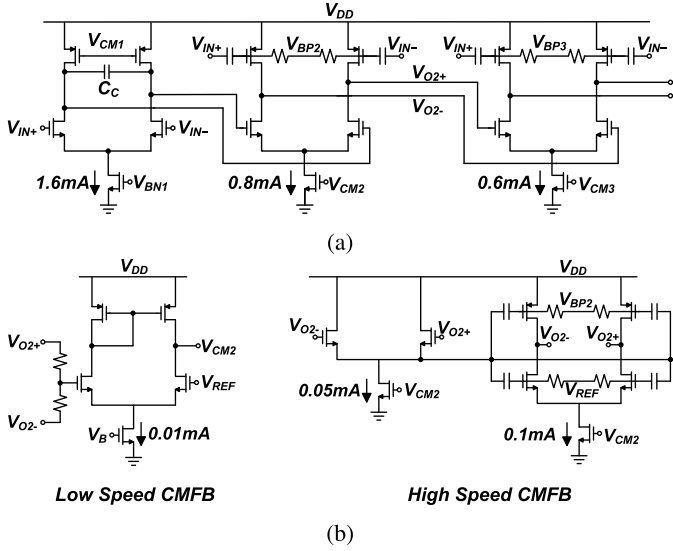
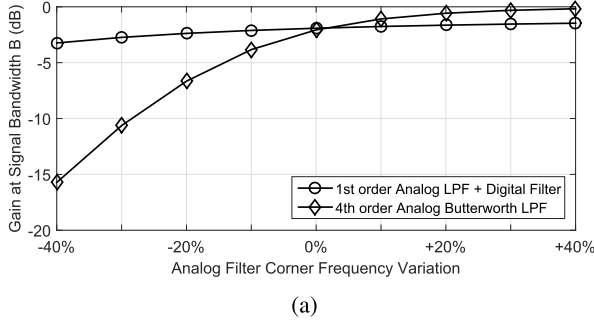
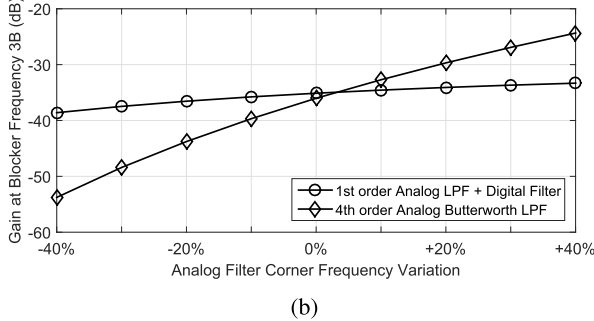


Fig. 16. Schematic of (a) third-order feedforward amplifier and (b) low-speed and high-speed CMFB circuit for the second stage.



(a)



(b)

Fig. 17. Simulated gain variations at (a) signal bandwidth B and (b) blocker frequency 3B.

differential pair similar to the one used in the second stage. The high-speed CMFB circuit is only needed in one stage as it provides sufficient protection against high-frequency common mode noise.

The baseband transfer function is very accurate as it is determined mainly by the digital filter coefficients and clock frequency. On the other hand, a higher order analog filter (for example, the fourth-order Butterworth filter in [6]) requires accurate tuning of  $R$  and  $C$ . Even though the first-order passive analog LPF is used in this paper, it does not need tuning. Fig. 17 compared the simulated variations in baseband gain for the proposed digital filtering ADC and a fourth-order

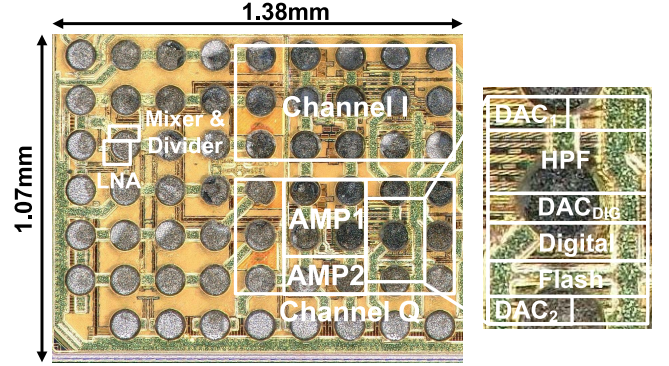


Fig. 18. Die photo.

analog Butterworth LPF. If the analog filter corner frequency varies  $\pm 40\%$ , the gain at signal bandwidth B only changes by 2 dB for this paper compared with 16 dB if a fourth-order analog Butterworth LPF is used for blocker rejection [see Fig. 17(a)]. The gain at a blocker frequency of 3B changes by 5 dB for this paper compared with 30 dB for the fourth-order analog Butterworth LPF [see Fig. 17(b)]. With process and temperature variations, the metal–oxide–metal capacitor value in 28-nm CMOS can vary by  $\pm 20\%$ , and poly resistors vary by  $\pm 15\%$ . Even excluding the switches, making  $R$  and  $C$  tunable presents at least 15%–20% area overhead, as well as increases complexity for calibration. A digital filter is also much easier to port into newer CMOS technologies and will benefit from scaling.

## V. MEASUREMENT RESULTS

The RF RX front-end prototype was fabricated in 28-nm CMOS technology. It occupies  $1.07 \text{ mm} \times 1.38 \text{ mm}$  with an active area of  $0.64 \text{ mm}^2$  (see Fig. 18). In this prototype, part of the blocker detection digital circuitry was implemented off-chip in MATLAB, as shown previously in Fig. 7(b). If implemented on-chip, the total digital area will increase by 15% and the power consumption of these digital logic will be minimal as the blocker detection algorithm is only active for a maximum of  $26 \mu\text{s}$  every 1 ms.

The measurement result is summarized and compared with other DSM-based RX designs in Table I. All measurements are performed with maximum gain setting (44 dB) controlled by the VGA unless otherwise specified. The RX front end operates at 0.9 and 1.8 GHz with a noise figure (NF) of 3.8 and 3.9 dB, respectively. The NF is measured by integrating the noise from 45 kHz to 9 MHz with the digital filter turned on. The RF front end (LNA+mixer) accounts for 82% of the total RX noise, and the baseband adds 18% which is dominated by the integrator. The RF front end in this paper was not optimized for this application and resulted in a poor NF but with a much smaller power consumption compared to [6]. It is worth noting that [6] has on-chip single-ended to differential conversion in the LNA, whereas the differential input RF front end used in this paper needs an external balun which further increases the NF by roughly 1.2 dB.

TABLE I  
MEASUREMENT SUMMARY AND COMPARISON  
TABLE WITH OTHER DSM-BASED RXs

	[6]	[17]	[18]	[19]	This work
Architecture	RX with $\Delta\Sigma$ -CSF	RX with filtering ADC	Direct $\Delta\Sigma$ RX	Direct $\Delta\Sigma$ RX	<b>RX with <math>\Delta\Sigma</math>-fb digital filter</b>
CMOS Technology (nm)	65	80	65	40	<b>28</b>
RF Frequency (GHz)	0.6-3	0.04-1	0.4-4	0.7-2.7	<b>0.9</b>
NF(dB)	2.4-3.5	2.7-3.5	16	5.9-8.8	<b>3.8</b>
Power (mW)	35.5-53 43.4@1.8GHz <sup>1</sup>	221.4	17-70.5 37.8@1.8GHz <sup>2</sup>	90	<b>19.5-36.6</b>
Power Breakdown (mW)	RF <sup>3</sup> BB Analog BB Digital	23.5-36.7 12-16.3 -	113.4 108 -	48 42 -	<b>4.4</b>
Supply (V)	1.2	1.8/1	1.5/1.2	1.1	<b>0.9</b>
IIP3 (dBm)	-6	-13	13.5	-2	<b>-7</b>
SNDR (dB)	45-52		52-68	40-43	<b>48</b>
RF Carrier BW (MHz)	10,20,40	5.6,7.8	4,10	1.4,15	<b>18</b>
Area (mm <sup>2</sup> )	0.7	5.6 <sup>4</sup>	0.56	1	<b>0.64</b>

1. LTE20 mode 2. Estimated 3. RF power includes LNA, mixer, LO gen and distribution  
4. Incl. PLL and DSP

The baseband digital consumes as little as 0.5 mW with no blockers present, 11.7 mW with only TX leakage cancellation on, and 17.6 mW with both TX leakage and blocker cancellation enabled, and hence the total power consumption for 1.8-GHz input can vary between 20.4 and 37.5 mW. IIP3 is measured with two blockers at 17.5 and 35 MHz, in accordance with the LTE20 standard [10]. The programmable notch was placed at 17.5 MHz, thus canceling most of the intermodulation product. IIP3 is  $-5$  dBm at 1.8 GHz. The baseband is very linear in the presence of blockers due to the digital blocker cancellation path; therefore, IIP3 is dominated by the RF front end.

Fig. 19 shows the measured output spectrum of channel I in four different scenarios for band 20 of the LTE20 standard. Note that the thermal noise is dominated by the RF front end. With the maximum gain setting,  $-48$  dBm at the RX input translates to  $0$  dBFS at the ADC input. First, in Fig. 19(a), the desired signal (SIG) is at  $-3$  dBFS. Since there are no blockers present, the digital filter can be turned off to provide a 45% power savings. Second, a  $+15$  dBFS CW TX leakage is present at 41-MHz frequency offset from the input and the desired signal is  $-20$  dBFS. The digital bandpass filter is turned on and placed exactly at 41 MHz to provide an attenuation of  $34.9$  dB [see Fig. 19(b)]. With the digital filter OFF, the ADC saturates as expected. Furthermore, in addition to the TX leakage, a  $+5$  dBFS blocker is introduced at 22.5 MHz and is attenuated by  $24.7$  dB by the programmable filter, as shown in Fig. 19(c). Finally, Fig. 19(d) shows the ADC output spectrum with a  $-47$  dBm modulated blocker at 22.5 MHz and a  $-34$  dBm modulated TX leakage at 41 MHz as required by the LTE20 standard [10]. Both blockers are produced by PRBS9 data patterns modulated with 16QAM at a bandwidth of 5 MHz. The resulting input to the RX has a peak envelope power of  $-26$  dBm. The modulated blocker at 22.5 MHz is attenuated by  $17.3$  dB and the modulated TX leakage is attenuated by  $31.5$  dB.

Fig. 20 shows the measured baseband frequency response with different settings for the programmable notch. It can be

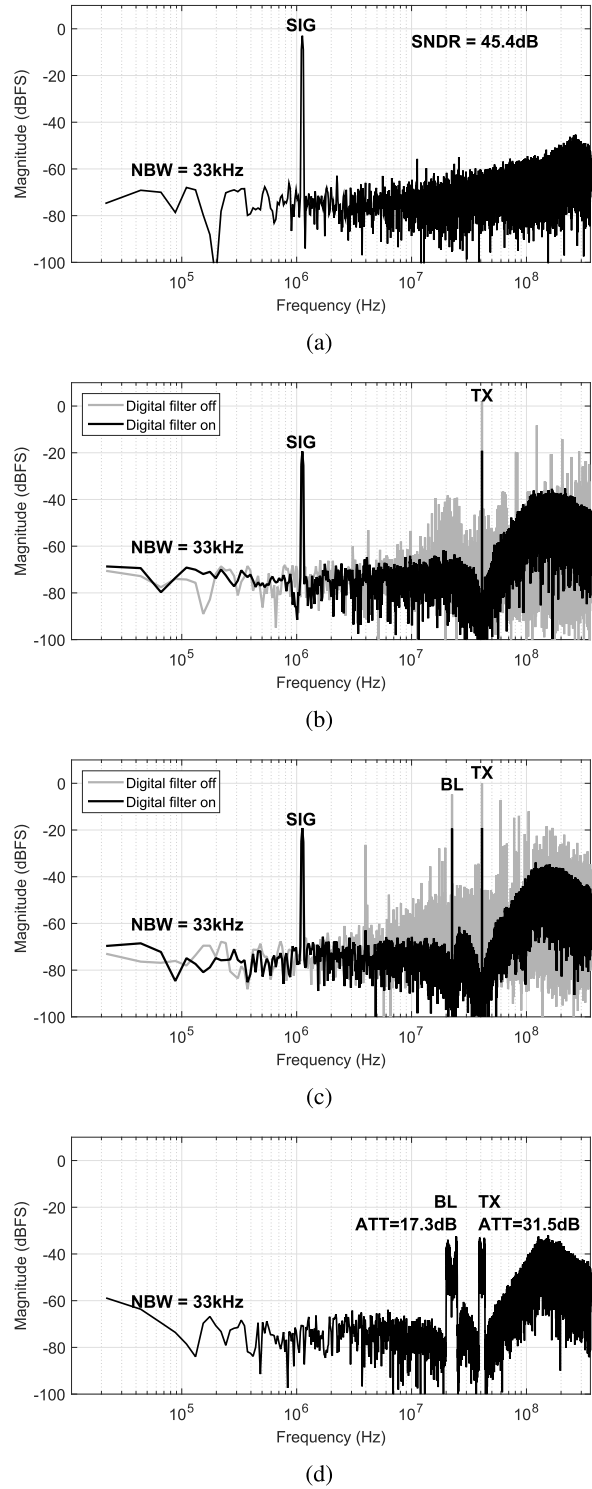
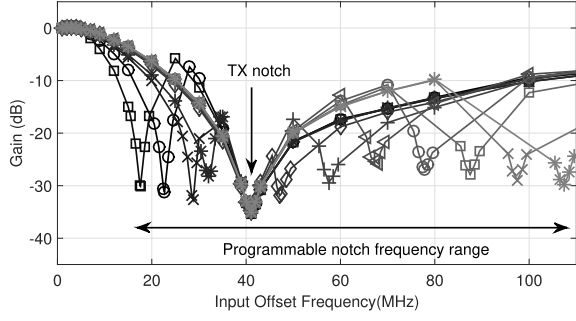
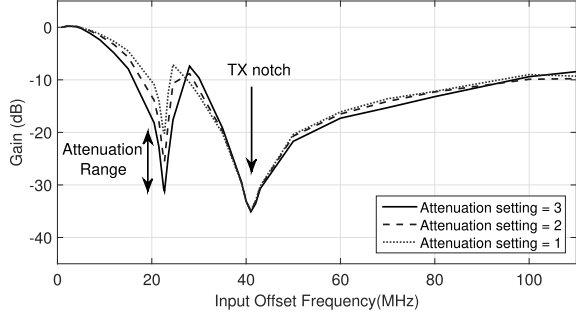


Fig. 19. Measured FFT spectrum for (a) no blocker, (b) CW TX leakage only, and (c) CW TX leakage and additional blocker, and (d) modulated TX leakage and additional blocker.

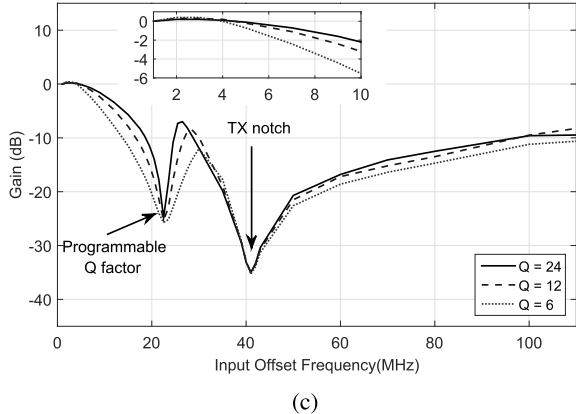
moved to any frequency in the range of  $17.5$ – $107.5$  MHz, as shown in Fig. 20(a). The minimum frequency step size is  $1$  MHz. The amount of attenuation can be decreased in  $6$  dB steps to increase the loop phase margin [see Fig. 20(b)]. The  $Q$  factor of the notch can be adjusted depending on the modulated blocker bandwidth, as shown in Fig. 20(c). A low  $Q$  notch is undesirable near the signal band to prevent signal attenuation;



(a)



(b)

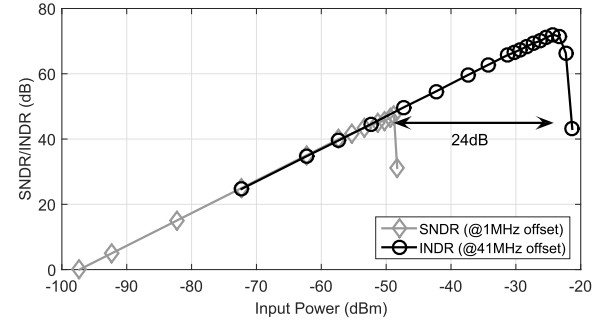


(c)

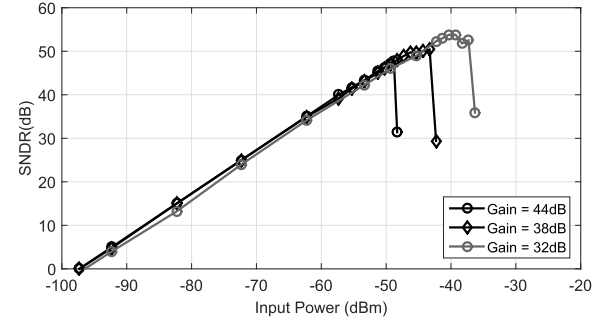
Fig. 20. Measured baseband frequency response for programmable notch at different (a) frequency, (b) attenuation, and (c)  $Q$  factor settings.

however, that is not a problem as blockers close to the signal band have a maximum bandwidth of 5 MHz [10].

Signal-to-noise and distortion ratio (SNDR) is measured with a signal input offset 1 MHz from the carrier, and the interference-to-noise and distortion ratio (INDR) is measured at 41-MHz offset, as shown in Fig. 21(a). The INDR is defined as the power ratio between the interferer at the input and the in-band noise. It can be seen that the RX front end can handle a TX leakage 24 dB larger than the ADC full scale, while maintaining the same in-band noise. The SNDR is plotted with different gain settings in Fig. 21(b). The RX gain is digitally programmable in 1 dB steps via the VGA from 32 to 44 dB. The dynamic range improves at lower gain settings,



(a)



(b)

Fig. 21. (a) SNDR and INDR at maximum gain setting versus RF input power. (b) SNDR at different gain settings versus RF input power.

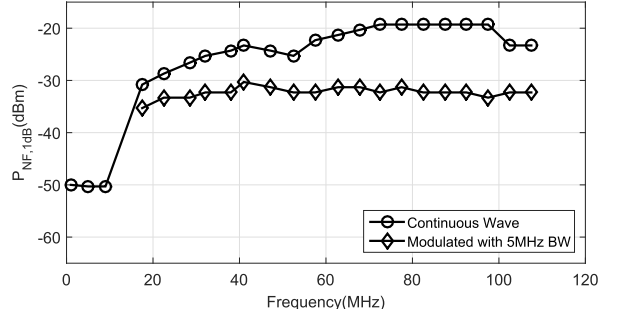


Fig. 22.  $P_{NF,1\text{ dB}}$  versus frequency for a CW blocker and a modulated blocker with 5-MHz bandwidth.

whereas the NF remains the same at 44 and 38 dB gain settings, and degrades by 1 dB at 32 dB gain.

For CW and modulated blockers with 5-MHz bandwidth,  $P_{NF,1\text{ dB}}$  is measured as the input blocker power when the NF increases by 1 dB (see Fig. 22). The modulated blocker used in this test has a peak-to-average power ratio of 9.5 dB, which is 6.5 dB higher than the CW blocker. The RX has great rejection for nearby blockers, just as expected. It can tolerate a  $-31 \text{ dBm}$  ( $+18 \text{ dBFS}$ ) CW blocker at 17.5 MHz, which is less than twice the signal bandwidth.

Measured operation of the blocker detection algorithm is shown in Fig. 23. In the beginning, the blocker is at  $-12 \text{ dBFS}$  and the RX is healthy with an SNDR of 30 dB at a signal amplitude of  $-20 \text{ dBFS}$ . At iteration 7, a large blocker ( $+7 \text{ dBFS}$ ) appeared and the SNDR is reduced to 10 dB due to RX saturation. The algorithm first increases the ADC full scale and then initiates the blocker detection algorithm

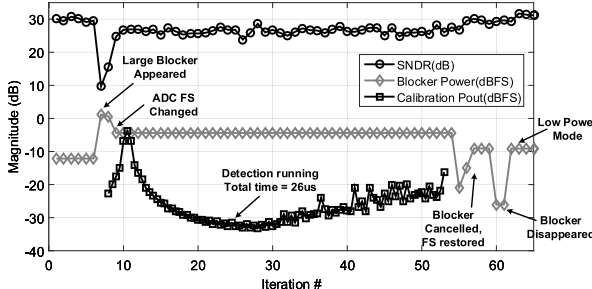


Fig. 23. Measured blocker detection algorithm.

that sweeps the programmable filter center frequency from 17.5 to 107.5 MHz in 1 MHz steps. The detection finishes at iteration 54 with a total time of 26  $\mu$ s. With the blocker frequency known, it is canceled and the ADC full scale is restored. It can be seen that around iteration 58, the SNDR rises to 30 dB again. At iteration 60, the blocker disappeared and low power mode is activated, which turns off the digital filter to save power.

## VI. CONCLUSION

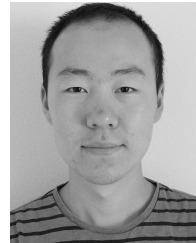
An RF RX with a multi-blocker canceling baseband is introduced as a replacement for the conventional cascade of an analog filter and ADC. The digital bandpass filters produce two flexible notches in the baseband frequency response, canceling TX leakage and an additional blocker as required by the LTE20 standard. Compared with previous state-of-the-art designs, this paper achieves competitive IIP3 and NF, while consuming the lowest power and can dynamically scale its power depending on the number of blockers present.

## ACKNOWLEDGMENT

The authors would like to thank Analog Devices for fabricating and packaging the chip, and provision of test equipment.

## REFERENCES

- [1] K. Philips *et al.*, “A continuous-time  $\Sigma\Delta$  ADC with increased immunity to interferers,” *IEEE J. Solid-State Circuits*, vol. 39, no. 12, pp. 2170–2178, Dec. 2004.
- [2] R. Rajan and S. Pavan, “Design techniques for continuous-time  $\Delta\Sigma$  modulators with embedded active filtering,” *IEEE J. Solid-State Circuits*, vol. 49, no. 10, pp. 2187–2198, Oct. 2014.
- [3] M. Sosio, A. Liscidini, R. Castello, and F. De Bernardinis, “A complete DVB-T/ATSC tuner analog base-band implemented with a single filtering ADC,” in *Proc. IEEE ESSCIRC*, Sep. 2011, pp. 391–394.
- [4] M. Sosio, A. Liscidini, and R. Castello, “A 2G/3G cellular analog baseband based on a filtering ADC,” *IEEE Trans. Circuits Syst. II, Exp. Briefs*, vol. 59, no. 4, pp. 214–218, Apr. 2012.
- [5] M. Andersson, M. Anderson, L. Sundström, S. Mattisson, and P. Andreani, “A filtering  $\Delta\Sigma$  ADC for LTE and beyond,” *IEEE J. Solid-State Circuits*, vol. 49, no. 7, pp. 1535–1547, Jul. 2014.
- [6] X. Liu *et al.*, “A 65 nm CMOS wideband radio receiver with  $\Delta\Sigma$ -based A/D-converting channel-select filters,” *IEEE J. Solid-State Circuits*, vol. 51, no. 7, pp. 1566–1578, Jul. 2016.
- [7] R. Ritter, P. Torta, L. Dörrer, A. Di Giandomenico, S. Herzinger, and M. Ortmanns, “A multimode CT  $\Delta\Sigma$ -modulator with a reconfigurable digital feedback filter for semi-digital blocker/interferer rejection,” in *Proc. IEEE ESSCIRC*, Sep. 2015, pp. 225–228.
- [8] R. Ritter, J. G. Kauffman, J. Becker, and M. Ortmanns, “A 10 MHz bandwidth, 70 dB SNDR continuous time delta-sigma modulator with digitally improved reconfigurable blocker rejection,” *IEEE J. Solid-State Circuits*, vol. 51, no. 3, pp. 660–670, Mar. 2016.
- [9] Q. Wang, H. Shibata, A. C. Carusone, and A. Liscidini, “A LTE RX front-end with digitally programmable multi-band blocker cancellation in 28 nm CMOS,” in *Proc. IEEE CICC*, Apr./May 2017, pp. 1–4.
- [10] *User Equipment (UE) Radio Transmission and Reception (Release 11)*, document 3GPP TS 36.101 V11.6.0 (2013-10), 2013.
- [11] E. Dahlman, S. Parkvall, and J. Skold, *4G: LTE/LTE-Advanced for Mobile Broadband*. San Diego, CA, USA: Academic, 2011.
- [12] H. Sun, A. Nallanathan, C.-X. Wang, and Y. Chen, “Wideband spectrum sensing for cognitive radio networks: A survey,” *IEEE Wireless Commun.*, vol. 20, no. 2, pp. 74–81, Apr. 2013.
- [13] X. Li, S. Shekhar, and D. J. Allstot, “ $G_m$ -boosted common-gate LNA and differential Colpitts VCO/QVCO in 0.18- $\mu$ m CMOS,” *IEEE J. Solid-State Circuits*, vol. 40, no. 12, pp. 2609–2619, Dec. 2005.
- [14] I. Fabiano, M. Sosio, A. Liscidini, and R. Castello, “SAW-less analog front-end receivers for TDD and FDD,” *IEEE J. Solid-State Circuits*, vol. 48, no. 12, pp. 3067–3079, Dec. 2013.
- [15] S. Yan and E. Sanchez-Sinencio, “A continuous-time  $\Sigma\Delta$  modulator with 88-dB dynamic range and 1.1-MHz signal bandwidth,” *IEEE J. Solid-State Circuits*, vol. 39, no. 1, pp. 75–86, Jan. 2004.
- [16] Y. Dong *et al.*, “A 930 mW 69 dB-DR 465 MHz-BW CT 1–2 MASH ADC in 28 nm CMOS,” in *ISSCC Dig. Tech. Papers*, Feb. 2016, pp. 278–279.
- [17] J. Greenberg *et al.*, “A 40-MHz-to-1-GHz fully integrated multistandard silicon tuner in 80-nm CMOS,” *IEEE J. Solid-State Circuits*, vol. 48, no. 11, pp. 2746–2761, Nov. 2013.
- [18] C. Wu, E. Alon, and B. Nikolić, “A wideband 400 MHz-to-4 GHz direct RF-to-digital multimode  $\Delta\Sigma$  receiver,” *IEEE J. Solid-State Circuits*, vol. 49, no. 7, pp. 1639–1652, Jul. 2014.
- [19] M. Englund *et al.*, “A programmable 0.7–2.7 GHz direct  $\Delta\Sigma$  receiver in 40 nm CMOS,” *IEEE J. Solid-State Circuits*, vol. 50, no. 3, pp. 644–655, Mar. 2015.



**Qiwei Wang** (S’13) received the M.A.Sc. degree from the Department of Electrical and Computer Engineering, University of Toronto, Toronto, ON, Canada, in 2013, where he is currently pursuing the Ph.D. degree.

His research interests include oversampling and time-interleaved analog-to-digital converters.



**Hajime Shibata** (S’99–M’02) received the B.E. and M.E. degrees in electrical engineering from the University of Electro-Communications, Tokyo, Japan, in 1997 and 1999, respectively, and the Dr. Eng. degree from the Tokyo Institute of Technology, Tokyo, in 2002.

Since 2002, he has been with Analog Devices, Toronto, ON, Canada, where he is involved in continuous-time  $\Delta\Sigma$  and continuous-time pipeline analog-to-digital converter designs.

Dr. Shibata was a co-recipient of the Beatrice Winner Award at ISSCC 2006.



**Antonio Liscidini** (S'99–M'06–SM'13) was born in Tirano, Italy, in 1977. He received the Laurea (*summa cum laude*) and Ph.D. degrees in electrical engineering from the University of Pavia, Pavia, Italy, in 2002 and 2006, respectively.

He was a summer Intern with National Semiconductors, Santa Clara, CA, USA, in 2003, studying poly phase filters and CMOS low-noise amplifiers. From 2008 to 2012, he was an Assistant Professor with the University of Pavia and a Consultant with Marvell Semiconductors, Pavia, in the area of integrated circuit design. In 2012, he moved to the Edward S. Rogers Sr. Department of Electrical and Computer Engineering, University of Toronto, Toronto, ON, Canada, where he is currently an Associate professor. His research interests include the implementations of transceivers and frequency synthesizers for cellular and ultra low power applications.

Dr. Liscidini was a recipient of the Best Student Paper Award at the IEEE 2005 Symposium on VLSI Circuits and a co-recipient of the Best Invited Paper Award at the 2011 IEEE Custom Integrated Circuit Conference. From 2008 to 2011, he served as an Associate Editor for the IEEE TRANSACTIONS ON CIRCUITS AND SYSTEMS II: EXPRESS BRIEFS, and he served as a Guest Editor for the IEEE JOURNAL OF SOLID-STATE CIRCUITS in 2013 and 2016. Since 2016, he has been a Distinguished Lecturer of the IEEE Solid-State Circuits Society. From 2012 to 2016, he was member for the TPC of the International Solid-State Circuit Conference. Currently, he is a member of the TPC of the European Solid-State Circuit Conference.



**Anthony Chan Carusone** (S'96–M'02–SM'08) received the Ph.D. degree from the University of Toronto, Toronto, ON, Canada, in 2002.

Since 2002, he has been with the Department of Electrical and Computer Engineering, University of Toronto, where he is currently a Professor. He is also an occasional consultant to industry in the areas of integrated circuit design and digital communication.

Dr. Chan Carusone currently serves as a member of the Technical Program Committee of the International Solid-State Circuits Conference. He has co-authored the best student papers at the 2007, 2008, and 2011 Custom Integrated Circuits Conferences, the Best Invited Paper at the 2010 Custom Integrated Circuits Conference, the Best Paper at the 2005 Compound Semiconductor Integrated Circuits Symposium, and the Best Young Scientist Paper at the 2014 European Solid-State Circuits Conference. He also co-authored, along with D. Johns and K. Martin, the second edition of the textbook *Analog Integrated Circuit Design*. He was the Editor-in-Chief for the IEEE TRANSACTIONS ON CIRCUITS AND SYSTEMS II: EXPRESS BRIEFS in 2009, an Associate Editor for the IEEE JOURNAL OF SOLID-STATE CIRCUITS from 2010 to 2017, and has served on the technical program committees for the Custom Integrated Circuits Conference, and the VLSI Circuits Symposium. He was a Distinguished Lecturer of the IEEE Solid-State Circuits Society from 2015 to 2017.